S. Rein

Lifetime Spectroscopy

A Method of Defect Characterization in Silicon for Photovoltaic Applications

Springer

Springer Series in
MATERIAL SCIENCE

Editors: R. Hull   R. M. Osgood, Jr.   J. Parisi   H. Warlimont

The Springer Series in Materials Science covers the complete spectrum of materials physics, including fundamental principles, physical properties, materials theory and design. Recognizing the increasing importance of materials science in future device technologies, the book titles in this series reflect the state-of-the-art in understanding and controlling the structure and properties of all important classes of materials.

Volumes 20–70 are listed at the end of the book.

S. Rein

Lifetime Spectroscopy

A Method of Defect Characterization
in Silicon for Photovoltaic Applications

With 153 Figures and 29 Tables

Springer

Dr. Stefan Rein
Fraunhofer Institute for Solar Energy Systems
Department Solar Cells, Materials and Technology
Heidenhofstr. 2, 79110 Freiburg, Germany
E-mail: stefan.rein@ise.fraunhofer.de

Series Editors:

Professor Robert Hull
University of Virginia
Dept. of Materials Science and Engineering
Thornton Hall
Charlottesville, VA 22903-2442, USA

Professor R. M. Osgood, Jr.
Microelectronics Science Laboratory
Department of Electrical Engineering
Columbia University
Seeley W. Mudd Building
New York, NY 10027, USA

Professor Jürgen Parisi
Universität Oldenburg, Fachbereich Physik
Abt. Energie- und Halbleiterforschung
Carl-von-Ossietzky-Strasse 9–11
26129 Oldenburg, Germany

Professor Hans Warlimont
Institut für Festkörper-
und Werkstofforschung,
Helmholtzstrasse 20
01069 Dresden, Germany

To my parents, my wife and my children,
with my love.

Preface

The monograph deals with lifetime spectroscopy, a group of new spectroscopic techniques to characterize defects in semiconductor materials. Electrically active defects may limit the performance of many semiconductor devices even if they are present in concentrations below the detection limit of conventional techniques. An important example concerns the energy conversion efficiency of solar cells. The development of strategies to reduce or avoid such harmful defects must start with their identification, which becomes increasingly difficult as the electronic quality of the semiconductor material improves. Because of its high sensitivity to all electrically active – and thus relevant – defects, lifetime spectroscopy is ideally suited for such an identification. This is reflected in the rapidly growing interest in lifetime spectroscopy which can be observed in the photovoltaic field.

Although the first publications on lifetime spectroscopy date back to the early 1990s, the potential of lifetime spectroscopy had not yet been analyzed systematically, which led to incorrect estimates even among specialists. In the present monograph, the possibilities and limitations of the different lifetime spectroscopic techniques are investigated in depth within a detailed theoretical evaluation, which allows the spectroscopic potential of the various techniques to be accurately assessed for the first time. Verification of the theoretical predictions within a comprehensive experimental study on different, technologically relevant metal impurities is another priority and demonstrates the usefulness of the different lifetime spectroscopic techniques as diagnostic tools. Finally, the successful characterization of the metastable defect in Czochralski silicon, which is well known due to its harmful impact on solar cell efficiency but could not previously be detected by any conventional technique, demonstrates the applicability of lifetime spectroscopy in practice.

Since the monograph thus covers the relevant topics of theoretical evaluation, experimental verification and application in practice, it represents a complete course on lifetime spectroscopy which may be interesting for different groups of readers. On the one hand, it is intended as an introduction to this field, with a uniform presentation of the techniques, a detailed physical explanation of all observed effects and a comprehensive

development of the theoretical results. The illustration of these results is based on a newly developed type of diagram – the defect parameter solution surface (DPSS) – which represents one of the key concepts of the work as it clearly visualizes the spectroscopic potential of the different techniques and thereby enables immediate understanding. Basic knowledge in the field of carrier lifetime and lifetime measurement techniques is helpful but not essential, as the basics are summarized in the first two chapters. Since lifetime measurements already represent a standard tool for process control in the photovoltaics industry, the monograph aims to deepen the reader's understanding of the complex quantity, carrier lifetime, and to stimulate its spectroscopic analysis.

On the other hand, the monograph is intended as a reference book for scientists and engineers who are actively involved in semiconductor material characterization and defect engineering in research institutes and industrial laboratories. Chapter and section summaries as well as detailed tabular overviews of the theoretical, methodological and experimental results allow both quick access to the major results and simple location of detailed information in the text. As the data evaluation technique proposed here not only gives deeper insight into the analytical potential of the different techniques but also allows the precision and consistency of lifetime spectroscopic results to be estimated quantitatively, it represents a very versatile tool which may set a new standard. Since there is a growing demand for increasingly sensitive techniques to trace ever-diminishing quantities of impurities due to the increasingly stringent requirements of electronic devices, it appears certain that lifetime spectroscopy will become widespread not only in photovoltaics but also in other branches of the semiconductor industry. Furthermore, as the methodological results of the monograph are completely detached from the technique used for the lifetime measurements, they form a general basis for a spectroscopic evaluation of lifetime data and are thus expected to stimulate new developments in different fields of material characterization.

Freiburg
December 2004   *Stefan Rein*

Contents

Abbreviations, acronyms and symbols

Abbreviations and acronyms

Acronym	Description
AM	air mass
arb.	arbitrary
Av	average
B, B_i, B_s	boron, interstitial boron, substitutional boron
BGN	band gap narrowing
BGH, BH	band gap half
B_iO_i	defect complex of boron and oxygen
B_sO_{2i}	defect complex of boron and an oxygen dimer
BSF	back surface field
B_sX	defect complex of boron and an unknown component X
C_s	substitutional carbon
CB	conduction band
CE	Coulomb enhancement
CP133	damage etch
CV	capacitance voltage
Cz	Czochralski (silicon)
DLTS	deep-level transient spectroscopy
DPSS	defect parameter solution surface
DPSS-DG	DPSS definition gap
DPSS-IP	DPSS intersection point
DPSS-PL	DPSS plateau value
DPSS-VR	DPSS validity range
DPSS-ZP	DPSS zero point
EM	effective mass
Fe, Fe_i	iron, interstitial iron
FeB	iron-boron pair
FTIR	Fourier transform infrared spectroscopy
FZ	float zone (silicon)
Ga	gallium
HLI	high-level injection
HT	high temperature
IC	intrinsic conduction

IDLS	injection-dependent lifetime spectroscopy
ISE	Fraunhofer Institute for Solar Energy Systems
LLI	low-level injection
LS	lifetime spectroscopy
LSF	least squares fit
LT	low temperature
MajBH	band gap half close to the majority band
mc	multicrystalline (silicon)
MCz	magnetic Czochralski (silicon)
MinBH	band gap half close to the minority band
MLI	mid-level injection
Mo	molybdenum
MW-PCD	microwave-detected photoconductance decay
N_{dop}-IDLS	injection-dependent lifetime spectroscopy at various doping conc.
Ni	nickel
O_i	interstitial oxygen
O_{2i}	oxygen dimer
PC1D	semiconductor device simulation software
PECVD	plasma-enhanced chemical vapor deposition
PT100	platinum temperature sensor
QSSPC	quasi-steady-state photoconductance
RCA	cleaning procedure for the silicon surface
REDR	recombination-enhanced defect reaction
RP-PERC	random pyramid passivated emitter and rear cell
RT	room temperature
Si	silicon
SRH	Shockley-Read-Hall
SRV	surface recombination velocity
TDLS	temperature-dependent lifetime spectroscopy
Ti	titanium
T-IDLS	injection-dependent lifetime spectroscopy at various temperatures
V	vacancies
VB	valence band
X	unknown defect component

Arabic symbols

Symbol	Description	Unit
$a, b, c \ldots i$	numerical constants in the effective mass model	—
B	coefficient of radiative band-to-band recombination	$cm^3 s^{-1}$
C	pre-factor to determine $[Fe]_{total}$ from lifetime data	$cm^{-3} s$
C_1	numerical constant in the FeB equilibrium fraction	cm^3

C_2	numerical constant in the FeB pair association time	$cm^{-3}K^{-1}s$
C_a	ambipolar Auger coefficient	cm^6s^{-1}
C_n, C_p	Auger coefficients	cm^6s^{-1}
$C_n{}^*, C_p{}^*$	Auger coefficients including Coulomb interaction	cm^6s^{-1}
c_n, c_p	capture coefficients for electrons and holes	cm^3s^{-1}
$c_n{}^*, c_p{}^*$	capture rates for electrons and holes	s^{-1}
Chi^2	error of a least squares fit	—
$(Chi^2)^{DPSS}$	error of a least squares fit (fitted DPSS parameter: DPSS-Chi^2 curve)	—
D	diffusivity	cm^2s^{-1}
D_a, D_n, D_p	ambipolar, electron, hole diffusion constant	cm^2s^{-1}
D_{it}	interface trap density	$cm^{-2}eV^{-1}$
D_C, D_V	density of allowed states in the CB and VB	$cm^{-3}eV^{-1}$
E	energy	eV
E_A, E_D	energy level of the dopant, acceptors and donors	eV
E_{ann}	activation energy, defect annihilation process in Cz-Si	eV
E_C	conduction band edge	eV
E_C-E_t	defect energy depth from the CB (true defect parameter)	eV
$(E_C-E_t)^{BEST}$	defect energy depth (optimum TDLS fit result for varied N_{dop})	eV
$(E_C-E_t)^{DPSS}$	defect energy depth (varied DPSS parameter: DPSS energy)	eV
$(E_C-E_t)^{DPSS-DG}$	definition gap of the DPSS-k curve related to IDLS (DPSS characteristic)	eV
$(E_C-E_t)^{DPSS-ZP}$	zero point of the DPSS-k curve related to IDLS (DPSS characteristic)	eV
$(E_C-E_t)^{DG/DPSS-ZP}$	definition gap of the DPSS zero-point function (DPSS characteristic)	eV
$(E_C-E_t)^{DPSS-IP\ 1,2}$	energy positions of the 1st/2nd DPSS-IP in a superposed DPSS-k diagram associated with a set of IDLS curves	eV
E^{corr}	energy correction term at the 2nd DPSS-IP in a superposed DPSS-k diagram associated with a set of IDLS curves	eV
E_{diss}	activation energy for the dissociation of iron-boron pairs	eV
E_F	Fermi energy	eV
$E_F{}^{Adv}$	Fermi energy, on the basis of the advanced T-model	eV
$E_F{}^{Stand}$	Fermi energy, on the basis of the standard T-model	eV
E_{gap}, E_{gap}^{300K}	energy band gap, at 300 K	eV
E_{gap}^{Green}	energy band gap, T-dependent according to Green	eV
E_{gap}^{Sze}	energy band gap, T-dependent according to Sze	eV
E_{gen}	activation energy, defect generation process in Cz-Si	eV
E_i	intrinsic Fermi energy	eV

E_{mig}	diffusion barrier of interstitial iron	eV
E_t	defect energy level (true defect parameter)	eV
E_V	valence band edge	eV
e_n, e_p	emission rates for electrons and holes	s^{-1}
E_∞	activation energy, multiphonon emission capture process	eV
f	Fermi-Dirac distribution function	—
f, g, h	functional interrelations	—
f_A	ionization degree, fraction of ionized acceptor atoms	—
FF	fill factor	—
f_{abs}	absorption fraction	—
f_i	intrinsic excitation degree, $p_0(T)/N_A$	—
f_t	probability of occupation of a defect level by an electron (Fermi-Dirac distribution function)	—
g_{eeh}, g_{ehh}	enhancement factors of the *eeh-* and *ehh*-Auger process	—
G	generation rate	cm^{-3}s^{-1}
G_0	generation rate in thermal equilibrium	cm^{-3}s^{-1}
G_{bulk}	bulk generation rate	cm^{-3}s^{-1}
h	Planck's constant	Js
I_{av}	illumination intensity	mW/cm^2
I_{bias}	intensity of the bias light	mW/cm^2
I_{deg}	intensity of the degradation light	mW/cm^2
J_n	electron current density	mA/cm^2
J_{SC}	short-circuit current density	mA/cm^2
$J_{SC,0}$	short-circuit current density, initial value in Cz-Si	mA/cm^2
$J_{SC,d}$	short-circuit current density, stable degraded value in Cz-Si	mA/cm^2
k	defect symmetry factor $k := \sigma_n/\sigma_p$ (true defect parameter)	—
k_B	Boltzmann's constant	eV/K
k^{BEST}	defect symmetry factor (optimum TDLS fit result for varied N_{dop})	—
k^{DPSS}	defect symmetry factor (fitted DPSS parameter: DPSS-k curve)	—
$k^{DPSS-IP}$	defect symmetry factor at the 1st/2nd DPSS-IPs in a superposed DPSS-k diagram associated with a set of IDLS curves	—
$k^{DPSS-PL}$	symmetry factor of the DPSS plateau region (DPSS characteristic)	—
m_e^*, m_h^*	effective mass of electrons and holes	—
m_l	numerical constant in the effective mass model	—
m_0	electron rest mass in the effective mass model	—
N	electron density in non-equilibrium	cm^{-3}
n_0	electron density in thermal equilibrium	cm^{-3}

n_1	electron SRH density	cm^{-3}
n_1^{DPSS}	electron SRH density (varied DPSS parameter)	cm^{-3}
$n_1^{DPSS-DG}$	electron SRH density related to the DPSS-DG energy	cm^{-3}
$n_1^{DPSS-ZP}$	electron SRH density related to the DPSS-ZP energy	cm^{-3}
$n_1^{DG/DPSS-ZP}$	electron SRH density related to the definition-gap energy of the DPSS-ZP function	cm^{-3}
$n_{1,trap}$	SRH density associated with a trapping center	cm^{-3}
n_i, n_i^{300K}	intrinsic carrier concentration, T-dependent and at $300\,K$	cm^{-3}
N_s	electron density at the surface	cm^{-3}
n_{s0}	electron density at the surface in thermal equilibrium	cm^{-3}
N	numerical factor of the effective density of states	cm^{-3}
N_A, N_D	concentration of dopant atoms, acceptors and donors	cm^{-3}
N_A^-, N_D^+	concentration of dopant atoms, ionized	cm^{-3}
N_A^0, N_D^0	concentration of dopant atoms, non-ionized	cm^{-3}
N_C, N_V	eff. density of states, in the CB and VB	cm^{-3}
N_C^{300K}, N_V^{300K}	eff. density of states, at $300\,K$	cm^{-3}
N_C^{PC1D}, N_V^{PC1D}	eff. density of states, with $T^{3/2}$-dependence	cm^{-3}
N_C^{EM}, N_V^{EM}	eff. density of states, based on the effective mass model	cm^{-3}
N_{crit}	critical recombination center density, validity limit of standard SRH theory due to internal trapping	cm^{-3}
N_{crit}^{LLI}	critical recombination center density, lower bound of N_{crit}	cm^{-3}
N_{dop}	doping concentration	cm^{-3}
N_{onset}	doping reference point (empirical bulk lifetime model)	cm^{-3}
N_{ph}^{1sun}	density of photons in solar light with 1 sun irradiance	cm^{-2}s^{-1}sun^{-1}
N_T	density of trapped excess electrons	cm^{-3}
N_t	defect concentration (conc. of recombination centers)	cm^{-3}
N_t^*	normalized defect concentration	cm^{-3}
N_{tA}, N_{tP}	concentration of the Cz defect, in the active state (A) and in the passive state (P)	cm^{-3}
$N_{t,norm}$	[B$_s$]-normalized defect concentration	cm^{-3}
$N_{t,norm}^{LT}$, $N_{t,norm}^{HT}$	[B$_s$]-normalized defect concentration, in the starting material (LT) and in high-temperature-treated material (HT)	cm^{-3}
N_{trap}	density of trapping centers	cm^{-3}
p	hole density in non-equilibrium	cm^{-3}
p_0	hole density in thermal equilibrium	cm^{-3}
p_1	hole SRH density	cm^{-3}
p_1^{DPSS}	hole SRH density (varied DPSS parameter)	cm^{-3}
$p_1^{DPSS-DG}$	hole SRH density related to the DPSS-DG energy	cm^{-3}
$p_1^{DPSS-ZP}$	hole SRH density related to the DPSS-ZP energy	cm^{-3}
$p_1^{DG/DPSS-ZP}$	hole SRH density related to the definition-gap energy of the DPSS-ZP function	cm^{-3}

p_s	hole density at the surface	cm^{-3}
p_{s0}	hole density at the surface in thermal equilibrium	cm^{-3}
q	elementary charge	C
r	ratio N_C/N_V of the effective density of states at 300 K	—
R	recombination rate	cm^{-3}s^{-1}
R_0	recombination rate in thermal equilibrium	cm^{-3}s^{-1}
R_{ann}	defect annihilation rate in Cz-Si	s^{-1}
R_{gen}	defect generation rate in Cz-Si	s^{-1}
R_n	recombination activity of the Cz defect (passive state)	s^{-1}
R_P	recombination rate via the Cz defect (passive state)	cm^{-3}s^{-1}
S	surface recombination velocity	cm/s
S	solubility	cm^{-3}
t	time	s
T	temperature	K
T_0	transition temperature where the T-IDLS curves turn over	K
$T_<, T_>$	T range where the defect-dependent contribution to LLI-SRH lifetime is negligible ($<$) and dominant ($>$)	K
$T_{Arrh-Onset}$	onset temperature of the Arrhenius increase (TDLS)	K
$T_{Arrh-Onset}^{Advanced}$	onset temperature of the Arrhenius increase (TDLS), on the basis of the advanced T-model	K
T_{fit}	T range underlying the SRH modeling of a TDLS curve	K
T_{FO}	freeze-out temperature	K
T_H	selected temperature in the $T_>$ region	K
$T_{IC}, T_{IC-Onset}$	onset temperature of intrinsic conduction	K
$T_{IC}^{Adv}, T_{IC-Onset}^{Advanced}$	onset temperature of intrinsic conduction, on the basis of the advanced T-model	K
$T_{IC}^{Stand}, T_{IC-Onset}^{Standard}$	onset temperature of intrinsic conduction, on the basis of the standard T-model	K
T_{iso}	temperature of an isothermal annealing experiment	K
T_L	selected temperature in the $T_<$ region	K
T_{trans}	T range in-between $T_<$ and $T_>$	K
U	net recombination rate	cm^{-3}s^{-1}
U_{Auger}	net Auger recombination rate	cm^{-3}s^{-1}
U_{bulk}	net bulk recombination rate	cm^{-3}s^{-1}
U_{eff}	effective net recombination rate	cm^{-3}s^{-1}
U_{rad}	net radiative recombination rate	cm^{-3}s^{-1}
U_S	net surface recombination rate	cm^{-2}s^{-1}
U_{SRH}	net SRH recombination rate via defects	cm^{-3}s^{-1}
U_ν	net recombination rates of the individual mechanisms	cm^{-3}s^{-1}
U_1	activation energy, FeB equilibrium fraction	eV
U_2	activation energy, FeB pair association time	eV

V	ratio of the recombination activities of two defect levels	—
V/I	resistance	Ω
V_{OC}	open-circuit voltage	V
$V_{OC,0}$	open-circuit voltage, initial value in Cz-Si	V
$V_{OC,d}$	open-circuit voltage, stable degraded value in Cz-Si	V
v_{th}, v_{th}^{300K}	thermal velocity, T-dependent and at 300 K	cm/s
W	wafer thickness	cm
x, y	space coordinates	cm
X	systematic error in an identification of τ_{eff} with τ_{bulk}	%
$x^{A,B}, x^{D1,D2}$	pairs of indexes to distinguish the parameters of two different defects in a two-defect SRH fit	—
$x^{S1,S2}$	pair of indexes to distinguish the parameters of two solutions	—
X	lifetime weighting factor (two-defect fit)	—
X	[B_s] correlation exponent	—
X^{LT}, X^{HT}	[B_s] correlation exponent, in the starting material (LT) and in high-temperature-treated material (HT)	—
Y	[O_i] correlation exponent	—
Y_C, Y_R	[O_i] correlation exponent, determined on the complete data set (C) and on a reduced data set (R)	—
$Y_{MCz}, Y_{Cz,MCz}$	[O_i] correlation exponent, determined on a set of MCz samples and a set of Cz and MCz samples	—
Y^{LT}, Y^{HT}	[O_i] correlation exponent, in the starting material (LT) and in high-temperature-treated material (HT)	—
Z	[C_s] correlation exponent	—
[B_s]	concentration of substitutional boron	cm^{-3}
[B_s]$_{norm}$	concentration of substitutional boron, reference point for N_t normalization	cm^{-3}
[C_s]	concentration of substitutional carbon	cm^{-3}
[Fe]$_{total}$	total iron concentration	cm^{-3}
[Fe]$_{Av}$	total iron conc., average value over a Δn range	cm^{-3}
Δ[Fe]$_{Av}$	total iron conc., standard deviation over a Δn range	cm^{-3}
[FeB]	concentration of iron-boron pairs	cm^{-3}
[Fe$_i$]	concentration of interstitial iron	cm^{-3}
[Ga]	concentration of gallium	cm^{-3}
[Mo]	concentration of molybdenum	cm^{-3}
[Ni]	concentration of nickel	cm^{-3}
[O$_i$]	concentration of interstitial oxygen	cm^{-3}, ppma
[O$_i$]^{LT}, [O$_i$]^{HT}	concentration of interstitial oxygen, in the starting material (LT) and in high-temperature-treated material (HT)	cm^{-3}, ppma
[Ti]	concentration of titanium	cm^{-3}
[V]	concentration of vacancies	cm^{-3}

Greek symbols

Symbol	Description	Unit
α	correlation exponent of $R_{gen}(N_A)$, $\tau_{Cz}(N_A)$ and $\sigma(T)$	—
α	temperature coefficient of $E_{gap}(T)$	eV/K
β	correlation exponent of $R_{gen}(I_{deg})$	—
β	temperature offset of $E_{gap}(T)$	K
δG	photogeneration relative to bias point, trapping correction	$cm^{-3}s^{-1}$
$\delta(\Delta n)$	excess electron density relative to bias point, trapping corr.	cm^{-3}
ΔE_{active}, $\Delta E_{passive}$	defect energy depth of the Cz defect (active/passive state)	eV
ΔE_t, ΔE_t^{true}	defect energy depth relative to the closer band edge (true defect parameter)	eV
ΔE_t^{fit}	defect energy depth extracted from a linear TDLS fit	eV
ΔE_t^{IP-2}	defect energy depth extracted from the 2nd DPSS-IP	eV
ΔE_t^{max}	maximum overestimate of the true energy depth by the DPSS-ZP energy	eV
ΔG_{av}	generation rate, averaged over wafer thickness	$cm^{-3}s^{-1}$
$\Delta\eta$	efficiency difference before/after degradation in Cz-Si	%
ΔJ_{SC}	J_{SC} difference before/after degradation in Cz-Si	mA/cm^2
$\Delta_{rel}[k]$	relative standard deviation of the DPSS-k curves associated with a set of IDLS curves	%
Δn, Δp	excess electron density, excess hole density	cm^{-3}
Δn_{av}, Δp_{av}	excess electron/hole density, averaged over wafer thickness	cm^{-3}
Δn_{bias}	excess electron density at the bias point, trapping corr.	cm^{-3}
$\Delta n_{crossover}$	position of the crossover of the Fe$_i$- and FeB-dominated IDLS curves	cm^{-3}
Δn_{fit}	Δn range underlying the SRH modeling of an IDLS curve	cm^{-3}
Δn_{min}	minority carrier density proportional to the base-line photoconductance, trapping correction	cm^{-3}
Δn_s, Δp_s	excess electron/hole density at the surface	cm^{-3}
$\Delta\sigma$	excess photoconductance	Ω^{-1}
$\Delta\tau_{SRH}$	SRH lifetime difference under HLI and LLI (general)	s
$\Delta\tau_{SRH}^p$	SRH lifetime difference, in p-type	s
$\Delta\tau_{SRH}^{p,MajBH}$	SRH lifetime difference, in p-type for a MajBH defect	s
$\Delta\tau_{SRH}^{p,MinBH}$	SRH lifetime difference, in p-type for a MinBH defect	s
$\Delta T_{Arrh-Onset}$	width of the T range exhibiting the Arrhenius increase	K
ΔV_{OC}	V_{OC} difference before/after degradation in Cz-Si	mV
η	injection level	—
η	conversion efficiency	%
η_0	conversion efficiency, initial value in Cz-Si	%

η_d	conversion efficiency, stable degraded value in Cz-Si	%
η_{max}	conversion efficiency, theoretical limit	%
μ_n, μ_p	mobility of electrons and holes	$\mathrm{cm^2V^{-1}s^{-1}}$
Π	probability of defect transformation	—
ρ, ρ_{base}	specific base resistivity	$\Omega\mathrm{cm}$
σ	photoconductance	Ω^{-1}
σ	capture cross-section, uniform T-dependence of σ_n and σ_p	$\mathrm{cm^2}$
σ_0, σ_∞	capture cross-section, T-independent pre-factors	$\mathrm{cm^2}$
σ_n, σ_p	capture cross-section of electrons and holes	$\mathrm{cm^2}$
σ_{trap}	excess photoconductance due to traps	Ω^{-1}
τ	carrier recombination lifetime (lifetime)	s
τ_0	upper lifetime limit (empirical bulk lifetime model)	s
τ_0	initial lifetime in Cz-Si, after an annealing step	s
τ_0^{LLI}	lifetime under low-level injection, before dissociation of FeB pairs	s
τ_1^{LLI}	lifetime under low-level injection, after dissociation of FeB pairs	s
τ_A, τ_B	stable degraded lifetime in HT-treated Cz-Si, processes A and B	s
τ_a	asymptotic lifetime in a two-level system with one trapping and one recombination center	s
τ_{app}	trapping-affected apparent lifetime	s
τ_{assoc}	defect association time of FeB pairs	s
τ_{Auger}	Auger lifetime (Auger recombination lifetime)	s
τ_{Auger}^{HLI}	Auger lifetime under high-level injection	s
$\tau_{Auger}^{LLI,n}$, $\tau_{Auger}^{LLI,p}$	Auger lifetime under low-level injection, in n-/p-type	s
τ_{bulk}	bulk lifetime (bulk recombination lifetime)	s
τ_{bulk}^{LLI}	bulk lifetime under low-level injection	s
$\tau_{bulk,max}^{LLI}$	bulk lifetime under low-level injection, theoretical limit	s
$\tau_{CE-Auger}$	Coulomb-enhanced Auger lifetime	s
$\tau_{CE\,Auger}^{LLI,n}$, $\tau_{CE\,Auger}^{LLI,p}$	Coulomb-enhanced Auger lifetime under low-level injection, in n-/p-type	s
τ_{corr}	carrier lifetime after bias correction	s
τ_{Cz}	bulk lifetime due to recombination via the Cz defect	s
τ_d	stable degraded lifetime in Cz-Si, after illumination	s
$\tau_{d,fit}$	empirical fit of doping-dependent τ_d data	s
τ_{eff}	effective lifetime (effective recombination lifetime)	s
τ_{eff}^{LLI}, τ_{eff}^{HLI}	effective lifetime under low-/high-level injection	s
$\tau_{eff,diff}$	effective lifetime, differential	s
$\tau_{ExpTerm}$	defect-dependent contribution to LLI-SRH lifetime (Arrhenius term)	s

τ_i	stable degraded lifetime in as-grown Cz-Si	s
τ_{gen}	time constant of defect generation in Cz-Si	s
$\tau_{n0}, \tau_{n0}^{300K}$	electron capture time constant, T-dependent and at 300 K	s
$\tau_{p0}, \tau_{p0}^{300K}$	hole capture time constant, T-dependent and at 300 K	s
τ_{n0}^{DPSS}	electron capture time constant (fitted DPSS parameter: DPSS-τ_{n0} curve)	s
$\tau_{n0}^{DPSS}(T)$	DPSS-τ_{n0} curves of a T-IDLS experiment	s
$\tau_{n0}^{DPSS}(300K)$	DPSS-τ_{n0} curves of a T-IDLS experiment, normalized to 300 K	s
$\tau_{n0}^{DPSS-IP}$	values of the DPSS-τ_{n0} curve at the energy position of the DPSS-k intersection points	s
τ_{p0}^{DPSS}	hole capture time constant (fitted DPSS parameter: DPSS-τ_{p0} curve)	s
τ_{rad}	radiative lifetime (radiative recombination lifetime)	s
$\tau_{rad}^{LLI}, \tau_{rad}^{HLI}$	radiative lifetime under low-/high-level injection	s
τ_{res}	lifetime due to recombination via all residual recomb. channels except for SRH recomb. via the Cz defect	s
τ_{SRH}	SRH lifetime (Shockley-Read-Hall recomb. lifetime)	s
$\tau_{SRH}^{deep}, \tau_{SRH}^{shallow}$	SRH lifetime for a deep and a shallow energy level	s
$\tau_{SRH}^{LLI}, \tau_{SRH}^{HLI}$	SRH lifetime under low-/high-level injection (exact expression)	s
$\tau_{SRH}^{LLI,n}, \tau_{SRH}^{LLI,p}$	LLI-SRH lifetime, in n-/p-type	s
$\tau_{SRH}^{LLI,p,MajBH}$	LLI-SRH lifetime, in p-type for a MajBH defect	s
$\tau_{SRH}^{LLI,p,MinBH}$	LLI-SRH lifetime, in p-type for a MinBH defect	s
$\tau_{SRH,<}^{LLI}$	LLI-SRH lifetime, in the $T_<$ region	s
$\tau_{SRH,>}^{LLI}$	LLI-SRH lifetime, in the $T_>$ region (Arrhenius increase)	s
$\tau_{SRH}^{LLI,IC}$	LLI-SRH lifetime, in the T range of intrinsic conduction	s
$\tau_{surface}$	surface recombination lifetime	s
τ_{total}	total SRH lifetime (several defect centers)	s
τ_ν	lifetime of the individual recombination channels	s
τ^*	LLI-SRH lifetime, linearized T-dependence (simple procedure)	s
τ_{n0}^*	electron capture time, simulated T-dependence	s
τ^{**}	electron capture time, measured T-dependence	s
τ^{***}	LLI-SRH lifetime, linearized T-dependence (advanced procedure)	s

Introduction

Motivation

At present, 90 % of the solar cells fabricated worldwide are made of crystalline silicon. An important approach to reduce the costs of these cells is to increase their energy conversion efficiency. As efficiency is strongly related to material quality, the analysis of electrically active defects, which may be introduced during crystal growth or during the solar cell manufacturing process, is of special importance, since these defects in general limit the material quality.

The most important microscopic parameter to characterize material quality is carrier recombination lifetime. Although deep-level transient spectroscopy (DLTS) is accepted to be one of the most sensitive techniques to detect and analyze small concentrations of electrically active defects [1], defect concentrations below the detection limit of DLTS can still significantly affect carrier recombination lifetime. A prominent example of such a recombination-active defect is the metastable defect in industrially-used monocrystalline Czochralski silicon [2, 3]. Although this defect could not be detected up to now by means of DLTS, carrier lifetime decreases by 90 % of its initial value when the defect is activated, which leads directly to a relative efficiency loss of 10 % in high-efficiency solar cells. This example shows the high sensitivity of carrier lifetime to electrically active defects, and also the important impact bulk defects may have on solar cell efficiency. Another semiconductor device with a similar sensitivity to bulk defects is the dynamic random access memory chip (RAM), where material quality and thus carrier lifetime determine the refresh time [4].

An improvement of device performance requires the reduction or avoidance of such recombination-active defects, which in turn requires their identification in order to identify critical process steps and to provide a reasonable starting-point for process optimization. Apart from detecting the presence of recombination-active defects, lifetime measurements allow direct identification of impurities if the injection and temperature dependence of carrier lifetime is analyzed. The different approaches, which all

rely on standard Shockley-Read-Hall theory (SRH theory) [5, 6], are referred to as *lifetime spectroscopy* (LS). Beyond its extraordinary sensitivity, the principle advantage of lifetime spectroscopy over traditional defect-characterization techniques is that it uses the recombination process to analyze defect centers and thus provides insight into precisely those defects which are actually relevant to semiconductor devices such as solar cells and random-access memories.

Although lifetime spectroscopy has the potential to be one of the most sensitive diagnostic tools for the identification of impurities in semiconductors and although some LS techniques have already been reported in the literature, lifetime spectroscopy is not yet established as a standard technique for defect characterization, the analytical potential of most LS techniques being unclear so far.

However, interest in lifetime spectroscopy is growing fast. First, this is due to the improved boundary conditions for lifetime measurements achieved during the past years. On the one hand, several new contactless lifetime measurement techniques have been developed. Of these, the quasi-steady-state photoconductance technique, recently developed by Sinton and Cuevas [7] and already well established, is ideally suited to measure carrier lifetime over a broad injection range, thus facilitating the use of techniques based on injection-dependent lifetime spectroscopy. On the other hand, high-quality surface passivation has been developed, and this now allows reliable measurements of bulk recombination properties [8]. An important advantage of these passivation techniques, which are mostly based on silicon nitride, is the use of low-temperature processes, which ensures that there are no changes in the bulk properties during sample preparation.

Second, lifetime spectroscopy is gaining in importance as there is a growing demand for increasingly sensitive techniques to track ever diminishing quantities of impurities, which affect electronic devices due to the more and more stringent requirements on them. In integrated-circuit technology, for example, the tolerable levels of contamination are decreasing due to the decreasing dimensions. Rapidly diffusing metals, such as iron and copper, can limit device production yield by increasing the junction leakage current and degrading the dielectric properties of gate oxides, thus leading to breakdown [9]. In photovoltaics, as demonstrated in the initial example, an unknown intrinsic defect in Czochralski silicon and low concentrations of undetermined metal impurities in multicrystalline silicon limit the energy conversion efficiency.

Moreover, a closer examination of the defect properties known for the metal impurities reveals that, in spite of the intensive investigations, performed especially in the early 1980s, knowledge of most metal impurities is insufficient if one wants to assess their impact on recombination and solar cell performance. One problem is that most impurities exhibit different energy levels, which have been reported without giving any information about their effective recombination activity, as this information is not available if conventional techniques are used. Since lifetime spectroscopy uses the recombination process itself to identify the defects, it is expected to fill this gap.

Aims and outline

Covering the whole field of lifetime spectroscopy, the theoretical part of this monograph aims at the development and assessment of a variety of different lifetime spectroscopic techniques focusing on two issues: on the one hand, on a detailed theoretical evaluation of the spectroscopic potential of the different LS techniques and on the other hand, on the development of transparent data evaluation procedures to make the different LS techniques applicable as a diagnostic tool.

Experimental LS investigations on samples intentionally contaminated with known metal impurities aim to confirm the analytical potential predicted for the different LS techniques in order to demonstrate the general applicability of lifetime spectroscopy as a diagnostic tool. Moreover, these investigations aim to complete our knowledge of the defects related to the different metal impurities and in particular, to identify the recombination-active defect level, which is highly relevant for photovoltaics.

Experimental LS investigations performed on the undetermined metastable defect in Czochralski silicon aim at a determination of its electronic structure, which represents the ultimate test for the practical use of lifetime spectroscopy. Moreover, additional lifetime investigations should determine the major components of the defect as well as the physical mechanism of defect transformation.

Following these aims, the book is divided into five chapters:

Chapter 1 introduces some key concepts related to carrier lifetime and discusses different models for the temperature dependence of the fundamental semiconductor quantities, which will be used throughout the work.

Chapter 2 briefly describes the two photoconductance-based measurement techniques used in this work for lifetime measurements.

Chapter 3 presents the detailed theoretical investigations into the spectroscopic potential of lifetime spectroscopy and thus represents the core of the work. The different LS techniques are developed and analyzed in separate sections and finally compared in the chapter summary.

Chapter 4 applies lifetime spectroscopy to intentionally metal-contaminated silicon samples. A concise overview of the experimental and methodological results achieved by investigations into the individual metal impurities is given.

Chapter 5 focuses on the metastable defect in Cz silicon with special emphasis on the application of lifetime spectroscopy.

References

[1]   D.V. Lang, *Deep-level transient spectroscopy: a new method to characterize traps in semiconductors*, J. Appl. Phys. **45** (7), 3023–32 (1974).

[2]   H. Fischer and W. Pschunder, *Investigation of photon and thermal induced changes in silicon solar cells*, Proc. 10th IEEE PVSC (Palo Alto, California, USA, 1973), pp. 404–11.

[3]   S.W. Glunz, S. Rein, J.Y. Lee, and W. Warta, *Minority carrier lifetime degradation in boron-doped Czochralski silicon*, J. Appl. Phys. **90** (5), 2397–404 (2001).

[4]   F. Shimura, T. Okui, and T. Kusama, *Noncontact minority-carrier lifetime measurement at elevated temperatures for metal-doped Czochralski silicon crystals*, J. Appl. Phys. **67** (11), 7168–71 (1990).

[5]   W. Shockley and W.T.J. Read, *Statistics of the recombinations of holes and electrons*, Phys. Rev. **87** (5), 835–42 (1952).

[6]   R.N. Hall, *Electron-hole recombination in germanium*, Phys. Rev. **87**, 387 (1952).

[7]   R.A. Sinton and A. Cuevas, *Contactless determination of current-voltage characteristics and minority-carrier lifetimes in semiconductors from quasi-steady-state photoconductance data*, Appl. Phys. Lett. **69** (17), 2510–2 (1996).

[8]   J. Schmidt, *Untersuchungen zur Ladungsträgerrekombination an den Oberflächen und im Volumen von kristallinen Silicium-Solarzellen*, Dissertation, Universität Hannover (1998).

[9]   S. Johnston and R.K. Ahrenkiel, *Measurement of the temperature dependence of silicon recombination lifetimes*, Defect and Impurity Engineered Semiconductors II (Symposium) (Warrendale, PA, USA, 1998), pp. 607–12.

1. Theory of carrier lifetime in silicon

1.1 Introduction

As the name indicates, lifetime spectroscopy uses the recombination life-time for defect characterization. Since this lifetime is a complex quantity, its accurate measurement and interpretation are mandatory for a successful application of lifetime spectroscopy. Thus, the present chapter introduces some key concepts related to recombination lifetime that will be used throughout the work.

Section 1.2 first introduces the fundamental semiconductor quantities and presents a detailed discussion of the temperature dependence of the carrier densities which has a decisive impact on the temperature-dependent carrier lifetime, as will be shown theoretically and experimentally in Chaps. 3 and 4, respectively. The essential terms of *recombination* and *carrier lifetime* are then introduced in Sect. 1.3. Following that, Sect. 1.4 introduces the different recombination mechanisms in semiconductors and discusses their relative importance in crystalline silicon. Basically, they may be divided into intrinsic processes, which occur even in the ideal non-disturbed semiconductor, and into extrinsic processes, which are related to impurities or lattice defects. With the radiative and the Auger band-band recombination the two intrinsic processes of bulk recombination are presented in Sects. 1.4.1 and 1.4.2, respectively. The extrinsic recombina-tion via defects in the bulk is discussed in Sect. 1.4.3 on the basis of the statistics developed by Shockley, Read and Hall [1, 2]. As this theory forms the basis of lifetime spectroscopy, the concept of its derivation is briefly delineated, leading to the general expression for SRH lifetime which represents the starting point for the detailed theoretical investiga-tions in Chap. 3. Discussing the fundamental prerequisites of standard SRH theory, a useful criterion recently developed to control its validity is introduced [3]. Its application successfully proves the validity of standard SRH theory for the investigations of the present work. The fundamentals of recombination via defects at the wafer surface are then discussed in Sect. 1.4.4, including the basic mechanisms for reducing the surface recombination rate. The effective lifetime arising from the superposition of these recombination processes is discussed in Sect. 1.5. As the main topic

of the monograph is the characterization of bulk defects, the impact of surface recombination on the effective carrier lifetime is investigated quantitatively, to estimate the required surface passivation quality which allows the measured effective lifetime to be directly identified with bulk lifetime.

1.2 Fundamentals 1: basic and advanced models for the fundamental semiconductor quantities

Since the modeling of the temperature-dependent carrier lifetime turns out to be sensitive to the accurate number of electrons and holes per unit volume, the present section is dedicated to a detailed derivation of their exact temperature dependence, the description being performed on three levels of accuracy. To introduce the fundamental concepts, we first discuss the *basic model* which corresponds to the model generally applied in solar cell physics, based on a temperature-independent majority carrier density. The temperature dependence of the majority carrier density is incorporated in the *standard model*, which takes into account the effects of freeze-out at low temperatures and intrinsic conduction at high temperatures. Finally, the *advanced model* considers the effect of an advanced temperature model for the effective densities of states and takes into account the temperature dependence of the energy band gap. The impact of these models on the temperature dependence of carrier lifetime will be shown in Sects. 3.5 and 3.6. In Chap. 4 we will finally demonstrate that accurate modeling of the measured temperature dependence of carrier lifetime actually requires the advanced temperature model.

1.2.1 Intrinsic carrier concentration and doping: the basic model

The energy band structure of a semiconductor is characterized by a narrow forbidden band gap which separates the valence and the conduction band. The width of this energy gap is given by $E_{gap} := E_C - E_V$, with E_C and E_V being the bottom and top of the conduction and the valence band, respectively. The densities of allowed states in the conduction and the valence band show a characteristic energy distribution which is given by $D_C(E) \propto (m_e^*)^{3/2} \times (E - E_C)^{1/2}$ and $D_V(E) \propto (m_h^*)^{3/2} \times (E_V - E)^{1/2}$, respectively. Note, that m_e^* and m_h^* are the effective masses of electrons and holes, respectively, which incorporate the effect of a periodic lattice potential and typically differ from each other.

At $T = 0$, the allowed states in the valence band are completely occupied while those in the conduction band are empty. As temperature increases,

an increasing number of electrons is thermally excited across the energy gap into the conduction band. If the Pauli exclusion principle[1] is taken into account, the Fermi-Dirac distribution function

$$f(E) = \left[1 + \exp\left(\frac{E - E_F}{k_B T} \right) \right]^{-1}$$

(1.1)

is found to describe the occupation probability of the allowed electron states of any given energy E in thermal equilibrium. In Eq. (1.1) T is the absolute temperature, k_B Boltzmann's constant and E_F the Fermi energy. Using the density of allowed states in both bands $D_C(E)$ and $D_V(E)$ and the probability $f(E)$ of their occupation, the absolute electron and hole density in the conduction and the valence band can be calculated from

$$n = \int_{E_C}^{\infty} D_C(E) f(E) dE \quad \text{and} \quad p = \int_{-\infty}^{E_V} D_V(E) f(E) dE$$

(1.2)

respectively. The integration of these expressions is greatly simplified as long as the Fermi energy is several $k_B T$ distant from the band edges, i.e., $E_C - E_F \gg k_B T$ and $E_F - E_V \gg k_B T$, since the Fermi-Dirac distribution (1.1) may then be reduced to the Boltzmann distribution $f(E) = \exp[-(E - E_F)/k_B T]$. This prerequisite, which is characteristic of a *non-degenerate* semiconductor, will be assumed throughout the work and verified in retrospect.[2]

In thermal equilibrium the following expressions are thus gained from Eq. (1.2) for the electron concentration n_0 in the conduction band and the hole concentration p_0 in the valence band [4, p.18]:

$$n_0 = N_C \exp\left(-\frac{E_C - E_F}{k_B T} \right)$$

(1.3a)

$$p_0 = N_V \exp\left(-\frac{E_F - E_V}{k_B T} \right)$$

(1.3b)

---

[1]   The Pauli exclusion principle implies that each allowed state can be occupied by, at most, two electrons of opposite spin.

[2]   The critical parameters for a validation of this assumption are the doping concentration N_{dop} and the temperature T. In the present work carrier lifetime is measured on samples with doping concentrations from 10^{14}–10^{16} cm^{-3} in a temperature range from 100 to 600 K. In spite of the temperature-related increase of $k_B T$ from 9 to 52 meV, the assumption of *non-degeneracy* is valid in the whole parameter range of interest since the Fermi level is shifted towards mid-gap with increasing temperature (see Fig. 1.4).

As expected, n_0 and p_0 strongly depend on the Fermi level E_F and the temperature T. N_C and N_V are the effective densities of states in the conduction and the valence band, respectively. They depend on the effective masses of electrons and holes, respectively, and contain an additional weaker temperature dependence, which results directly from the integration of Eq. (1.2) and is given by [4, p.17]:

$$N_{C/V}(T;m^*_{e/h}) = N^{300K}_{C/V}(m^*_{e/h}) \times \left(\frac{T}{300K}\right)^{3/2} \tag{1.4}$$

If the product of the equilibrium carrier concentrations n_0 and p_0 is formed, a fundamental feature of carriers in a semiconductor is revealed, the so-called *law of mass action* of carriers [4, p.18]:

$$n_0 p_0 = N_C N_V \exp\left(-\frac{E_{gap}}{k_B T}\right) =: n_i^2 \tag{1.5}$$

In contrast to the equilibrium carrier concentrations themselves, their product $n_0 p_0$ no longer depends on the Fermi level E_F, but only on the temperature and doping-independent material parameters, which implies the introduction of a new material parameter n_i. Thus, irrespective of the doping level of a sample, the product of electron and hole density is constant ($n_0 p_0 = n_i^2$), provided that the semiconductor is in thermal equilibrium and non-degenerate.

A Intrinsic semiconductor

In the ideal case of an undoped (intrinsic) semiconductor, the thermal excitation of electrons into the conduction band can only occur from the valence band. As a consequence, the electron density in the conduction band equals the hole density in the valence band. Their common value corresponds to the material parameter n_i which is thus known as the intrinsic carrier concentration:

$$n_0 = p_0 = n_i \tag{1.6}$$

At 300 K a value of 10^{10} carriers per cm^3 has been determined for n_i [5]. If n_0 and p_0 in Eq. (1.6) are substituted by the expressions from Eqs. (1.3b) and (1.3a), we find an expression for the Fermi level E_F:

$$E_F - E_V \equiv E_i - E_V = \frac{E_{gap}}{2} - \frac{k_B T}{2}\ln\left(\frac{N_V}{N_C}\right) \tag{1.7}$$

Except for a small temperature-dependent correction term, which results from the numerical difference of the effective densities of states in the valence and the conduction band, the Fermi level in an intrinsic semiconductor, which is also known as *intrinsic energy E_i*, lies approximately in the middle of the forbidden band.

B Extrinsic semiconductor

However, in the case of a doped (extrinsic) semiconductor the position of the Fermi level and thus the equilibrium concentrations n_0 and p_0 of electrons and holes decisively depend on the type and the concentration of the dopant used.

For doping, the semiconductor is intentionally contaminated with special impurities which are incorporated substitutionally on lattice sites and form shallow energy levels in the band gap. Silicon as a group IV semiconductor can be doped with group III and group V elements. Since group V elements, such as phosphorus, form energy levels close to the conduction band edge, they easily donate their extra electron to the conduction band. They are thus known as donors and induce an *n*-doping. Analogous, group III elements, such as boron, are known as acceptors, since they form energy levels close to the valence band edge and thus easily accept an electron from this band. This increases the hole density in the valence band and thus induces a *p*-doping. In their ionized state, donors have a net positive and acceptors a net negative charge. In the following, N_A and N_D denote the total acceptor and donor densities while N_A^- and N_D^+ refer to their ionized fraction.

Typical doping concentrations N_{dop} range from 10^{13}–10^{20} dopant atoms per cm^3. Since N_{dop} is thus several orders of magnitude higher than the intrinsic carrier concentration n_i, the law of mass action (1.5) implies a separation of electrons and holes into majority and minority carriers. An approximate and simple calculation of the actual electron and hole densities in a doped semiconductor is based on two assumptions: (i) impurity depletion, i.e., the complete ionization of all dopant atoms, which implies $N_A^- \approx N_A$ and $N_D^+ \approx N_D$, respectively, and (ii) a negligible contribution of the intrinsic carrier concentration to the majority carrier concentration, i.e., $n_i \ll N_A$ and $n_i \ll N_D$, respectively. Since both assumptions are well fulfilled in a broad temperature range around room temperature, the approximation gives results of more than adequate accuracy in this temperature range. While the majority carrier concentration can thus be equated with the doping concentration, the corresponding minority carrier concentration has to be calculated from Eq. (1.5). This leads to
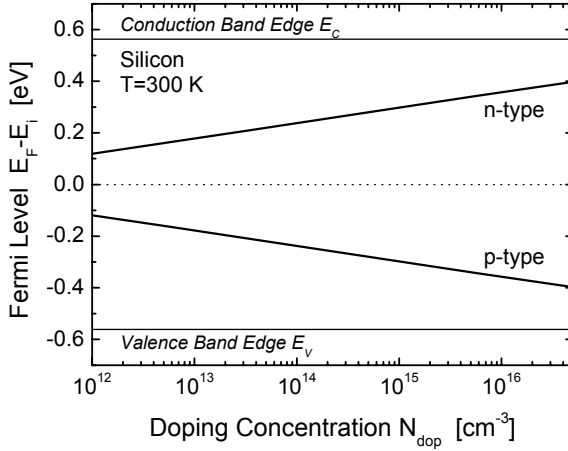
Fig. 1.1. Fermi level E_F as a function of doping concentration in *n*- and *p*-type silicon at 300 K according to Eq. (1.10). The dopant is assumed to be completely ionized (impurity depletion). As will be shown in Sect. 1.2.2A, this assumption is only valid at 300 K for $N_{dop} < 2.5 \times 10^{16}\,\mathrm{cm}^{-3}$.

$$p_0 = N_A \quad \text{and} \quad n_0 = \frac{n_i^2}{N_A} << p_0 \quad \text{for a } p\text{-type semiconductor,} \qquad (1.8a)$$

$$n_0 = N_D \quad \text{and} \quad p_0 = \frac{n_i^2}{N_D} << n_0 \quad \text{for an } n\text{-type semiconductor.} \qquad (1.8b)$$

Since Eqs. (1.3a) and (1.3b) for the equilibrium carrier concentrations n_0 and p_0 also apply for the more general case of a doped semiconductor, an expression for the position of the Fermi level can easily be derived:

$$E_F - E_V = k_B T \ln\left(\frac{N_V}{N_A}\right) \qquad \text{for a } p\text{-type semiconductor,} \qquad (1.9a)$$

$$E_C - E_F = k_B T \ln\left(\frac{N_C}{N_D}\right) \qquad \text{for an } n\text{-type semiconductor.} \qquad (1.9b)$$

Thus, in a doped semiconductor the position of the Fermi level is directly determined by the doping concentration. As displayed in Fig. 1.1, the Fermi level is shifted with increasing doping concentration towards the valence band edge in the case of a *p*-doped semiconductor and towards the conduction band edge in the case of an *n*-doped semiconductor. For symmetry reasons between *n*- and *p*-type, the Fermi levels in Fig. 1.1 are not calculated with respect to one of the band edges but with respect to the

intrinsic energy E_i, given in Eq. (1.7). The underlying expression can be directly derived if the Eqs. (1.9) are combined with Eq. (1.7). Note that the upper and the lower signs in Eq. (1.10) hold for a *p*-type and an *n*-type semiconductor, respectively:

$$E_F - E_i = \mp \frac{E_{gap}}{2} \pm k_B T \ln\left[\frac{(N_V N_C)^{1/2}}{N_{dop}}\right] \tag{1.10}$$

C Definition of the basic model

Based on these fundamental concepts, we now define the *basic model* for the temperature dependence of the semiconductor quantities as it will be used in Chaps. 3 and 4 for the calculation and modeling of carrier lifetime.

Concerning the equilibrium carrier concentrations, the fundamental assumption of the basic model is – as for the above derivation – a temperature-independent majority carrier concentration, which equals the doping concentration, e.g. in *p*-type: $p_0 = N_A$. In spite of the actual strong temperature dependence of the minority carrier concentration via $n_i(T)$ as described by Eq. (1.8), the minority carrier concentration is also considered as independent of the temperature in the basic model. It is calculated from Eq. (1.8) using the intrinsic carrier concentration at 300 K, e.g. in *p*-type: $n_0 = n_i^{300K}/N_A$. This additional simplification is introduced for the sake of consistency, since the temperature dependence of the minority carrier density only becomes important for the calculation of the carrier lifetime at temperatures where the majority carrier concentration changes as well. This will be shown in Sects. 1.2.2 and 1.2.3. The basic model is expected to give accurate results in a broad temperature range around room temperature where the above assumption is valid.

Although neglected in the calculation of p_0 and n_0, the simple $T^{3/2}$-dependence of the effective densities of states in the conduction and the valence band, which is displayed in Eq. (1.4), is considered whenever N_C and N_V appear in other quantities.

D Set of parameters used for simulations with the basic model

The set of material parameters used for theoretical calculations with the basic model is taken from the semiconductor-device-simulation program PC1D (version 5.8) [6]. A complete determination of the system is achieved if the following three material parameters are specified at 300 K:

$$E_{gap} \qquad = 1.124\,\text{eV} \qquad \text{energy band gap in silicon,}$$

$$n_i^{300\text{K}} \qquad = 1.0 \times 10^{10}\,\text{cm}^{-3} \quad \text{intrinsic carrier concentration [5]},$$

$$r := \frac{N_C^{300\text{K}}}{N_V^{300\text{K}}} \quad = 1.06 \qquad \text{ratio of the effective densities of states.}$$

Making use of Eq. (1.5), the effective densities of states in the valence and the conduction band can be directly calculated at 300 K:

$$N_C^{300\text{K}} = \left[r \left(n_i^{300\text{K}} \right)^2 \exp\left(\frac{E_{gap}}{k_B\,300\text{K}} \right) \right]^{1/2} = 2.84 \times 10^{19}\,\text{cm}^{-3},$$

$$N_V^{300\text{K}} = \left[\frac{1}{r} \left(n_i^{300\text{K}} \right)^2 \exp\left(\frac{E_{gap}}{k_B\,300\text{K}} \right) \right]^{1/2} = 2.68 \times 10^{19}\,\text{cm}^{-3},$$

with Boltzmann's constant given by $k_B = 8.62 \times 10^{-5}\,\text{eV/K}$.

1.2.2 Temperature dependence of the majority carrier concentration: the standard model

Up to now, the majority carrier concentration in a doped semiconductor has been regarded as temperature-independent, which allows the semiconductor to be accurately described around room temperature. Nevertheless, the underlying assumptions of (i) *impurity depletion* and (ii) a negligible contribution of *intrinsic conduction* become invalid at temperatures much lower and higher than 300 K, respectively.

In fact, at sufficiently low temperatures the fraction of ionized doping atoms is reduced due to the reduced energy available for thermal excitation, and impurity depletion is no longer given. As a result of this so-called *freeze-out* of the doping atoms the majority carrier concentration decreases with decreasing temperature. At sufficiently high temperatures on the other hand, the concentration of intrinsic carriers, which are thermally excited across the band gap, exceeds the doping concentration. As then even the doped semiconductor becomes dominated by intrinsic conduction, the majority carrier concentration is no longer constant but increases with increasing temperature. Concerning the temperature dependence of the majority carrier concentration, the temperature range thus displays a tripartition (for *p*-type) [4, p.26]:

$T = 0\text{–}150\,\text{K}$	region of *freeze-out*	$p_0(T) < N_A$,
$T = 150\text{–}500\,\text{K}$	region of *impurity depletion*	$p_0(T) = N_A$,
$T > 500\,\text{K}$	region of *intrinsic conduction*	$p_0(T) > N_A$.

Note that the transition temperatures strongly depend on the doping concentration, the given temperatures being valid for a doping level of approximately 10^{15} cm^{-3}.

Since the lifetime spectroscopic investigations in Chap. 4 are performed in a temperature range from 100 to 600 K, the temperature dependence of the majority carrier concentration is expected to affect the temperature-dependent lifetime curves. Although the temperature region of impurity depletion is most important for temperature-dependent lifetime spectroscopy, it will be shown in Sect. 3.5 and Chap. 4 that an accurate modeling of the lifetime curve over the whole temperature range increases the accessible spectroscopic information and significantly improves the accuracy of the spectroscopic result. Thus, an accurate calculation of the complete temperature dependence of the equilibrium carrier concentrations is indispensable. Here, we do not only focus on the derivation of the temperature dependence itself, but also on the exact determination of the transition temperatures between the three regions and their dependence on the doping concentration. The latter should demonstrate the relevance of improved temperature models in the investigated temperature range and allow an individual a priori identification of the critical temperature regions.

The general approach to determine the precise values for the electron and hole concentrations starts from the fundamental condition of charge neutrality. For example, for *p*-type material it takes the form

$$n_0(T) + N_A^-(T) = p_0(T) \tag{1.11}$$

which considers both the densities p_0 and n_0 of free carriers and the concentration N_A^- of negatively charged ionized acceptor atoms. Making use of the law of mass action (1.5), which is the second important equation, the minority carrier concentration n_0 can be written as function of p_0. As a result Eq. (1.11) becomes a quadratic equation in p_0 which provides the general solution for the majority carrier concentration $p_0(T)$:

$$p_0(T) = 1/2 \left[N_A^-(T) + \sqrt{N_A^-(T)^2 + 4\,n_i(T)^2} \right] \tag{1.12}$$

The majority carrier concentration thus depends on its intrinsic value $n_i(T)$ and on the unknown density N_A^- of ionized doping atoms. To arrive at an explicit expression for $p_0(T)$, Eq. (1.12) is analyzed in the following in the temperature regions of freeze-out and intrinsic conduction. The obtained partial solutions are then combined to a composite function which represents the general solution for $p_0(T)$.

A Freeze-out

At low temperatures, $N_A^-(T)$ strongly depends on temperature due to the above mentioned freeze-out of doping atoms. To allow the magnitude of the freeze-out effect to be assessed directly, the ionization degree f_A is introduced, which equals the fraction of ionized acceptor atoms and thus ranges below 1:

$$f_A(T) := N_A^-(T) / N_A \qquad (1.13)$$

Since $f_A(T)$ and $N_A^-(T)$ strongly depend on the Fermi level and the energy level of the acceptor atoms, respectively, the determination of their temperature dependence requires a physical model for the population of impurity levels in thermal equilibrium. As shown in the literature [7, p.581], the population statistics of impurity levels differ slightly from the common Fermi-Dirac statistics (1.1), since the population of localized states has to consider electron-electron interactions, which essentially prohibit the double occupation of donor levels by electrons and acceptor levels by holes.[3] The complete statistics provide the following expressions for the densities $N_D^0(T)$ and $N_A^0(T)$ of non-ionized donors and acceptors, respectively:[4]

$$N_D^0(T) = \frac{N_D}{1 + \dfrac{1}{2}\exp\!\left(\dfrac{E_D - E_F}{k_B T}\right)} \ , \quad N_A^0(T) = \frac{N_A}{1 + \dfrac{1}{2}\exp\!\left(\dfrac{E_F - E_A}{k_B T}\right)} \qquad (1.14)$$

with E_D and E_A denoting the energy level of the donors and acceptors, respectively. The combination of Eqs. (1.13) and (1.14) yields the functional dependence of f_A:

---

[3]   Donor levels for example can either be empty or occupied by one electron of either spin whereas a double occupation by electrons of opposite spin is essentially prohibited due to the mutual Coulomb repulsion. Acceptor levels on the other hand can either be singly or doubly occupied by electrons, but not empty, which can be explained as above from the hole point of view [7, p.581].

[4]   Actually, the population statistics yield expressions for the mean densities n_D and p_A of electrons in the donor levels and holes in the acceptor levels, respectively. But due to the maximum single-occupation of both types of levels, n_D and p_A can be directly identified with the densities N_D^0 of non-ionized donors (singly occupied by an electron) and N_A^0 of non-ionized acceptors (singly occupied by a hole), respectively. The difference in the maximum occupancy of localized (impurity) and delocalized (band) states is reflected in the factor of 1/2 in the denominators of Eq. (1.14).

$$f_A(T) := \frac{N_A^-(T)}{N_A} = \frac{N_A - p_A(T)}{N_A} = \left[1 + 2\exp\left(-\frac{E_F - E_A}{k_B T}\right)\right]^{-1} \qquad (1.15)$$

Since $f_A(T) \equiv f_A(T; E_F, E_A)$, the Fermi level E_F can be expressed as a function of the ionization degree f_A:

$$E_F(T; f_A, E_A) = E_A + k_B T \ln\left[\frac{2 f_A(T)}{1 - f_A(T)}\right] \qquad (1.16)$$

Nevertheless, since both quantities, f_A and E_F, are undetermined a priori, Eqs. (1.16) and (1.15) are of no direct use with regard to the explicit calculation of $p_0(T)$ for given material parameters. To overcome this problem, $E_F(T)$ has to be expressed in general terms as a function of the doping concentration N_A.

Such an expression follows directly from Eq. (1.12) which can be solved for E_F if $p_0(T)$ is given by Eq. (1.3a). In the temperature region of freeze-out, Eq. (1.12) simplifies and gives $p_0(T) \approx N_A^-(T) = f_A(T) \times N_A$ since the intrinsic carrier concentration n_i there can be neglected, provided that there is an extrinsic semiconductor: $n_i(T) \ll N_A, N_A^-$. Although it is not required for the derivation of E_F from a theoretical point of view, the use of the simplified Eq. (1.12) has the appeal that it simplifies the expression gained for E_F without loss of accuracy:

$$E_F(T; f_A, N_A) = E_V + k_B T \ln\left[\frac{N_V(T)}{f_A(T) N_A}\right] \qquad (1.17)$$

If either the two expressions (1.16) and (1.17) for the Fermi level are equated or the N_A-dependent expression (1.17) for the Fermi level is inserted in Eq. (1.15), an expression for the ionization degree $f_A(T)$ is gained after some rearranging, which only depends on temperature and known material parameters and thus allows a numerical calculation of $f_A(T)$ and $p_0(T)$, respectively:

$$f_A(T; N_A, E_A) = \frac{-1 + \sqrt{1 + 2\, C(T; N_A, E_A)}}{C(T; N_A, E_A)}$$

with $\qquad C(T; N_A, E_A) := \frac{4 N_A}{N_V(T)} \exp\left(\frac{E_A - E_V}{k_B T}\right) \qquad (1.18)$
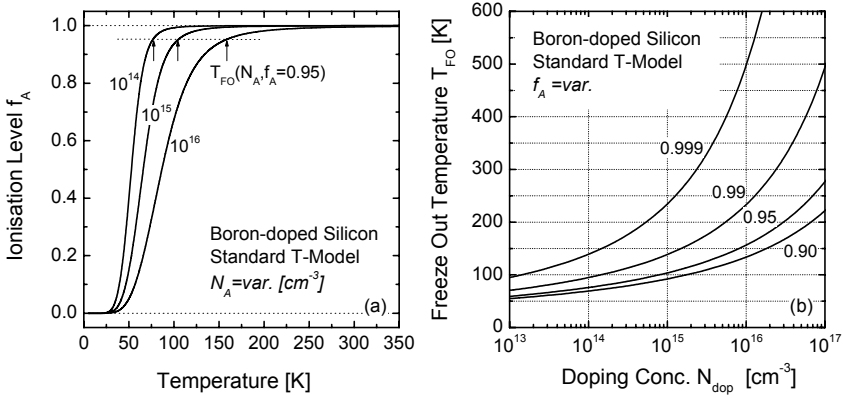
Fig. 1.2. (**a**) Ionization degree f_A of boron atoms in silicon as a function of temperature for different doping concentrations. *Arrows* indicate the T_{FO} positions for an f_A threshold of 0.95. (**b**) Freeze-out temperature T_{FO} in boron-doped silicon as a function of the doping concentration for different threshold limits of the ionization degree.

The ionization degree f_A of boron atoms in silicon, which form an energy level at E_A-$E_V = 0.045\,\text{eV}$ [4, p.21], is plotted in Fig. 1.2a as a function of temperature for different doping concentrations. As indicated by the arrows, the onset of freeze-out can be characterized by a transition temperature T_{FO} which strongly depends on the doping concentration N_A and the specified threshold value for the ionization level f_A (in Fig. 1.2a given by the dotted line at $f_A = 0.95$). Unfortunately, the derivation of an analytical expression for $T_{FO}(N_A;f_A)$ fails since Eq. (1.18) is unsolvable for temperature. Nevertheless, a graphical solution can be deduced insofar as an analytical expression for the inverse function $N_A(T_{FO};f_A)$ is derived from Eq. (1.18) which is then plotted in an $x(y)$- instead of a $y(x)$-plot. After some rearranging of Eq. (1.18) the result is: $\hspace{2cm}$ (1.19)

$$N_A(T_{FO};f_A) \equiv N_A(T_{FO},f_A,E_A) = \frac{1-f_A}{2f_A^2}\ N_V(T_{FO})\ \exp\!\left(-\frac{E_A-E_V}{k_B T_{FO}}\right)$$

Figure 1.2b displays the inverse function $T_{FO}(N_A;f_A)$ as a function of the doping concentration N_A for various ionization degrees f_A, again calculated for boron-doped silicon. As can be seen, the transition temperature T_{FO} increases with increasing doping concentration N_A. The fact that the freeze-out of doping atoms already occurs at higher temperatures in more highly doped material, originates from the reduced distance between Fermi and doping level, which results in a reduced ionization of the doping atoms. In addition Fig. 1.2b shows the strong dependence of transition temperature

T_{FO} on the ionization level f_A which is predefined as the threshold value for the transition from impurity depletion to freeze-out. If an ionization degree of 99 % is regarded as a sufficient criterion for impurity depletion, at a temperature of 300 K, samples up to a doping concentration of $2.5 \times 10^{16}\,\mathrm{cm^{-3}}$ can be treated in the limit of impurity depletion, which demonstrates that the freeze-out effect can be neglected at room temperature. In contrast, at 100 K, which corresponds to the lowest temperature worked at in the present study, the freeze-out effect has to be considered for samples doped as low as $10^{14}\,\mathrm{cm^{-3}}$, since for a medium doping concentration of, e.g., $10^{15}\,\mathrm{cm^{-3}}$, almost 10 % of the doping atoms are already frozen out at 100 K.

B Intrinsic conduction

At sufficiently high temperatures, the effect of thermally induced intrinsic conduction starts to dominate the majority carrier concentration $p_0(T)$. Since $n_i(300\,\mathrm{K}) = 10^{10}\,\mathrm{cm^{-3}}$ is several orders of magnitude smaller than the doping concentration, the transition from extrinsic to intrinsic conduction appears at temperatures much higher than 300 K, i.e., at temperatures for which impurity depletion can be assumed and thus $N_A^-(T) = N_A$. This assumption simplifies Eq. (1.12), which then allows the temperature-dependent majority carrier concentration $p_0(T)$ to be calculated directly if $n_i(T)$ is replaced by its defining expression (1.5). Figure 1.3a displays the majority carrier concentration $p_0(T)$ as a function of inverse temperature for various doping concentrations, showing the exponential increase due to intrinsic conduction at high temperatures.

Analogous to the freeze-out effect, the onset of intrinsic conduction can be characterized by a transition temperature T_{IC}, which is defined as the temperature at which the majority carrier concentration $p_0(T)$ exceeds the doping concentration N_A by a predefined factor $f_i > 1$. This factor can be interpreted as an intrinsic excitation degree:

$$p_0(T_{IC}) =: f_i \times N_A \tag{1.20}$$

The arrows in Fig. 1.3a indicate the T_{IC} positions for $f_i = 2$. As can be seen, the onset of intrinsic conduction is shifted to higher temperatures T_{IC} when doping concentration increases, which is reflected for more highly doped samples by a broadening of the temperature region, in which majority carrier concentration is dominated by extrinsic conduction and thus independent of temperature. An analytical expression for $T_{IC}(N_A; f_i)$ should follow from Eq. (1.12) for $N_A^-(T) = N_A$ and upon substitution of $p_0(T)$ from Eq. (1.20). But since Eq. (1.12) is again unsolvable for temperature, only an expression for the inverse function $N_A(T_{IC}; f_i)$ can be deduced:
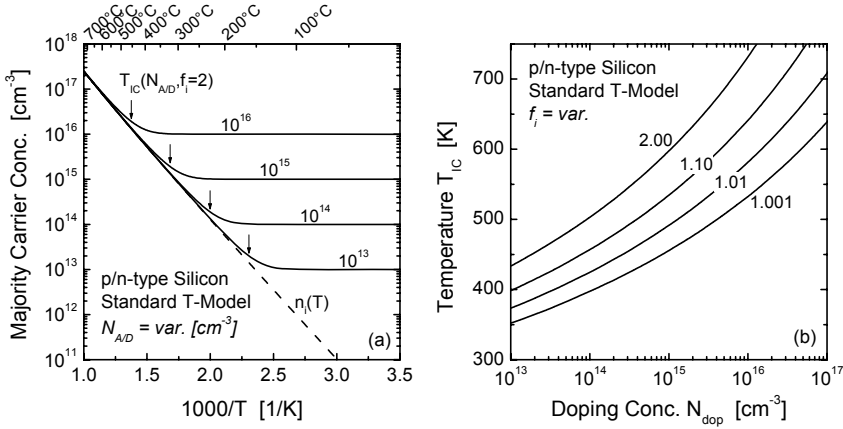
Fig. 1.3. (**a**) Majority carrier concentration as a function of inverse temperature for different doping concentrations, considering the effect of thermally induced intrinsic conduction according to Eq. (1.12) for $N_A^- = N_A$. The intrinsic carrier concentration $n_i(T)$ (*dashed line*) is calculated on the basis of the basic *T*-model according to Eq. (1.5). The temperature at which the majority carrier concentration $p_0(T)$ exceeds N_{dop} by a predefined factor $f_i > 1$ is defined as the onset temperature T_{IC} of intrinsic conduction. *Arrows* indicate the T_{IC} positions for $f_i = 2$. (**b**) Onset temperature of intrinsic conduction T_{IC} as a function of doping concentration for different transition factors f_i.

$$N_A(T_{IC}; f_i) = \frac{n_i(T_{IC})}{\sqrt{f_i^2 - f_i}} \qquad (1.21)$$

Equation (1.21) being plotted in an *x(y)*- instead of a *y(x)*-plot, Fig. 1.3b displays the onset temperature $T_{IC}(N_A; f_i)$ of intrinsic conduction as a function of the doping concentration N_A for different values for the factor f_i, again calculated for boron-doped silicon. As expected, the transition temperature T_{IC} is the lower the lower the doping concentration N_A and the lower the factor f_i, which is assumed as a threshold for the transition from extrinsic to intrinsic conduction. The significance of the doping dependence of T_{IC} becomes evident with a numerical example. If $f_i = 1.10$ is defined as the threshold for the transition to intrinsic conduction, a decrease in the doping concentration by only two orders of magnitude from 10^{16} to 10^{14} cm^{-3} results in a T_{IC} decrease by 180 K from 640 to 460 K. Thus at 600 K, which is the highest temperature worked at in the present study, the effect of intrinsic conduction has to be considered for samples up to a doping concentration of 5×10^{15} cm^{-3}, since for a lower doping concentration of, e.g., 10^{15} cm^{-3}, the intrinsic carrier density already exceeds the extrinsic carrier density by 100 % ($f_i = 2$).

C Fermi level in the standard model

Combining the results obtained in the region of freeze-out and intrinsic conduction, we are now able to define the *standard model* for the temperature dependence of the equilibrium carrier concentrations as it will be used in Chaps. 3 and 4 for the calculation and modeling of carrier lifetime.

Since, for the derivation of $p_0(T)$, we simplified the general Eq. (1.12) by neglecting the intrinsic carrier concentration $n_i(T)$ at low temperatures and by assuming $N_A^-(T) = N_A$ at high temperatures,[5] the general solution for the majority carrier concentration $p_0(T)$ has to be defined as a composite function of both partial solutions, which requires a suitable division of the temperature range. According to Figs. 1.2b and 1.3b, $T = 350\,\text{K}$ represents a suitable division temperature since there neither freeze-out nor intrinsic conduction affect semiconductors doped in a broad range from 1×10^{13} to $5 \times 10^{16}\,\text{cm}^{-3}$. Thus, the general temperature dependence of the majority carrier concentration $p_0(T)$ (in *p*-type material) may be written as

$$p_0(T) = \begin{cases} f_A(T)\,N_A & \text{for } T < 350°\text{C}, \\ 1/2 \times \left[N_A + \sqrt{N_A^2 + 4n_i(T)^2} \right] & \text{for } T \geq 350°\text{C}, \end{cases} \tag{1.22}$$

with the ionization degree $f_A(T)$ and the intrinsic carrier concentration $n_i(T)$ given by Eqs. (1.18) and (1.5), respectively. Both equations depend on the effective densities of states $N_C(T)$ and $N_V(T)$, whose temperature dependence is described by the simple $T^{3/2}$-dependence given in Eq. (1.4), which is used in the basic model as well. In contrast to the basic model, the standard model also considers the complete temperature dependence of the minority carrier concentration $n_0(T)$. Making use of the law of mass action (1.5), it directly results from $p_0(T)$ and $n_i(T)$:

$$n_0(T) = n_i(T)^2 / p_0(T) \tag{1.23}$$

Finally, we are now able to present a generalized expression for the Fermi level E_F, which considers both freeze-out and intrinsic conduction and thus allows its temperature dependence to be described completely. If the derivation given in Sect. 1.2.1B is followed, the resultant E_F expression for a *p*-type doping takes the form:[6]

---

[5] Note that neither simplification has been required from a theoretical point of view, but they led to a significant simplification of the resulting expressions without loss of accuracy in the temperature range of definition.

[6] In the case of an *n*-type doping, the general expression for the Fermi level simply follows from Eq. (1.24) if the whole expression is multiplied by the factor (1) and $p_0(T)$ is replaced by the majority carrier concentration $n_0(T)$, whose temperature dependence has to be derived analogously to Eq. (1.22).
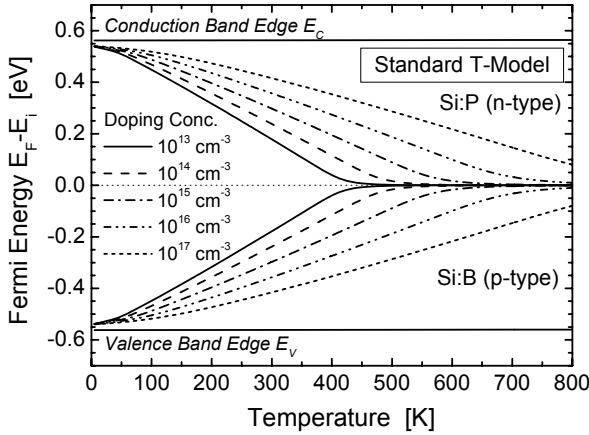
Fig. 1.4. Fermi level $E_F(T)$ as a function of temperature for *p*- and *n*-type silicon with different doping concentrations. For symmetry reasons the intrinsic Fermi level E_i (approximately mid-gap) is chosen as zero energy. The calculations are based on Eq. (1.24) considering both freeze-out and intrinsic conduction as described in the standard *T*-model.

$$E_F - E_i = -\frac{E_{gap}}{2} + k_B T \ln\left[\frac{(N_V N_C)^{1/2}}{p_0(T)}\right] \tag{1.24}$$

For symmetry reasons between *n*- and *p*-type, the Fermi level E_F is again calculated with respect to the intrinsic energy E_i. Note that the general E_F expression (1.24) only differs from the simple E_F expression (1.10) in that the direct doping dependence is replaced by a dependence on the temperature-dependent majority carrier concentration $p_0(T)$ given by Eq. (1.22).

Figure 1.4 displays the Fermi level calculated from Eq. (1.24) as a function of temperature for *n*- and *p*-type silicon with different doping concentrations. The discussed effects of freeze-out and intrinsic conduction are directly reflected in the observed temperature dependence of E_F. Irrespective of the doping concentration, the Fermi level is shifted with decreasing temperature towards the corresponding band edge which causes the freeze-out of doping atoms. With increasing temperature on the contrary, the Fermi level moves towards mid-gap. As soon as E_F reaches mid-gap, the doped semiconductor is completely dominated by intrinsic conduction and differences due to doping type and concentration disappear. Apart from that, the trends observed in Fig. 1.1 for the doping dependence of E_F are confirmed for arbitrary temperatures: the Fermi level E_F is located closer to the valence (in *p*-type) and the conduction band edge (in *n*-type) the higher the doping concentration.

1.2.3 Impact of advanced temperature models for $N_{C,V}(T)$ and $E_{gap}(T)$: the advanced model

As will be shown in Sect. 3.4 and Chap. 4, even the standard model does not allow the temperature-dependent lifetime curves to be modeled accurately. Since the intrinsic carrier concentration $n_i(T)$ and thus the equilibrium carrier concentrations $p_0(T)$ and $n_0(T)$ strongly depend on the values of E_{gap}, $N_C(T)$ and $N_V(T)$ as manifested in Eqs. (1.5), (1.22) and (1.23), further extensions of the temperature model for the fundamental semiconductor quantities arise from (i) a consideration of the temperature- and doping-induced narrowing of the silicon band gap and (ii) the use of advanced temperature models for the effective densities of states, which take into account an additional temperature dependence of the effective masses. In the following we briefly introduce these models, which are discussed in detail in [8], focussing (i) on their deviation from the more common simpler models and (ii) on their impact on the semiconductor quantities derived in the previous sections.

A Characteristics of the models

The band gap in silicon is known to decrease with increasing temperature. Its temperature dependence has been determined from the absorption edge of silicon and is accurately described in a T range from 0–1000 K by the following empirical equation published by Sze [4, p.15]:

$$E_{gap}(T) = E_{gap}(0) - \frac{\alpha T^2}{T + \beta} \tag{1.25}$$

with a zero-point energy gap $E_{gap}(0) = 1.170\,\text{eV}$, a temperature coefficient $\alpha = 4.73 \times 10^{-4}\,\text{eV/K}$ and a temperature offset $\beta = 636\,\text{K}$.

Figure 1.5a displays the temperature dependence of the energy band gap $E_{gap}(T)$ for the Sze model, calculated from Eq. (1.25) (solid line), as well as for a slightly modified model published by Green [9, p.60] (dash-dotted line). Although older, the Sze model[7] is preferred to the Green model since it provides the well determined value of 1.124 eV for the silicon band gap at 300 K. The deviation of the excluded E_{gap}-models, $E_{gap} = \text{const.}$ and $E_{gap}{}^{Green}$, from the Sze model, which is chosen as optimum, is displayed in Fig. 1.5b (lower half) in percentages. The deviation between $E_{gap} = \text{const.}$ and $E_{gap}{}^{Sze}$ (dashed line) demonstrates the relevance of considering the temperature dependence of E_{gap} which becomes evident by an E_{gap} shrinkage

---

[7] Note that in the semiconductor-device-simulation program PC1D (version 5.8) [6] the Sze model is also used to describe $E_{gap}(T)$.
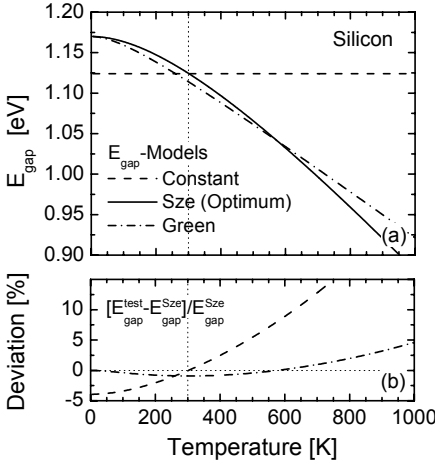
Fig. 1.5. (**a**) Temperature dependence of the energy band gap $E_{gap}(T)$ for different models. (**b**) Deviation in percentages of the excluded E_{gap}-models from the Sze model, which is chosen as optimum. While the deviation between $E_{gap} = $ const. and E_{gap}^{Sze} (*dashed line*) demonstrates the relevance of considering the temperature dependence of E_{gap}, the deviation between E_{gap}^{Green} and E_{gap}^{Sze} (*dash-dotted line*) is a measure of the uncertainty of the model used.

Fig. 1.6. (**a**) Absolute values of superposed doping-induced band gap narrowing (BGN) as a function of temperature for different doping concentrations in meV units. (**b**) Ratio of BGN and total band gap width in percentages. Since the ratio remains below 0.5 %, the impact of BGN on the total band gap width can be neglected in the present study.

of 10 % at 600 K compared to the value at 300 K. The deviation between E_{gap}^{Green} and E_{gap}^{Sze} (dash-dotted), on the contrary, is a measure for the uncertainty of the model used. In the relevant temperature range up to 650 K this uncertainty is below 1 % and can thus be neglected.

In addition, the band gap may be reduced due to the effect of doping-induced band gap narrowing (BGN), which is superimposed onto the pure temperature effect discussed above. Using the BGN model implemented in the semiconductor-device-simulation software DESSIS [10], we calculated the band gap narrowing as a function of temperature for different doping concentrations. The result is displayed in Fig. 1.6a in units of meV. As expected, the BGN increases with increasing doping concentration and decreasing temperature. To assess the relevance of BGN, Fig. 1.6b (lower half) shows the ratio of BGN and total band gap width in percentages. Since the ratio remains below 0.5 % in the relevant doping ($< 10^{16}$ cm^{-3}) and temperature (100–650 K) range and thus below the uncertainty of the $E_{gap}(T)$-model, the impact of BGN on the total band gap width can be neglected in the present study.

Finally, an advanced model for the temperature dependence of the effective densities of states, $N_C(T)$ and $N_V(T)$, should be introduced. The simple $T^{3/2}$-dependence, which has been found in Eq. (1.4), directly follows from the integration of the energy state density $D(E)$ within the integral (1.2) and does not consider any temperature dependence of the effective masses of electrons and holes. To account for such effects, the effective densities of states have to be written as [8]

$$N_{C/V}\left(T; \frac{m_{e/h}^*(T)}{m_0}\right) = N \times \left[\frac{m_{e/h}^*(T)}{m_0}\right]^{3/2} \times \left[\frac{T}{300\text{K}}\right]^{3/2} \tag{1.26}$$

where m_e^* and m_h^* are the effective masses of electrons in the conduction band and holes in the valence band, respectively, m_0 is the electron rest mass and $N = 2.541 \times 10^{19}\,\text{cm}^{-3}$ is a numerical factor, which collects all residual physical constants.

As discussed in [8], a change in the effective masses with temperature has to be expected from two effects. On the one hand, the energy-momentum curves themselves, from which the effective masses are deduced, change with temperature due to a change in the electron-phonon interaction energies. On the other hand, at increased temperatures, those regions of the bands are increasingly occupied which are away from the band edge and thus depart from simple parabolic shape. A multitude of experimental and theoretical results are found to be well described by the following equations for the effective masses m_e^* and m_h^* [8]:

$$\frac{m_e^*(T)}{m_0} = 6^{2/3}\left[\left(C\frac{E_{gap}(0)}{E_{gap}(T)}\right)^2 \frac{m_l}{m_0}\right]^{1/3} \tag{1.27a}$$

$$\frac{m_h^*(T)}{m_0} = \left(\frac{a + bT + cT^2 + dT^3 + eT^4}{1 + fT + gT^2 + hT^3 + iT^4}\right)^{2/3} \tag{1.27b}$$

The numerical values of the coefficients a–i, C and m_l/m_0 are given in [8] and displayed below.[8] The structural difference in the analytical expressions for the electron and hole effective mass results from differences in the band structure of the conduction and the valence band. This is why the effective mass of holes in the valence band is expected to be more temperature-sensitive than that of electrons in the conduction band [8].

---

[8] Coefficients in the EM equations (1.27) [8]: $C = 0.1905$, $m_l/m_0 = 0.9163$, $a = 0.4435870$, $b = 0.3609528 \times 10^{-2}$, $c = 0.1173515 \times 10^{-3}$, $d = 0.1263218 \times 10^{-5}$, $e = 0.3025581 \times 10^{-8}$, $f = 0.4683382 \times 10^{-2}$, $g = 0.2286895 \times 10^{-3}$, $h = 0.7469271 \times 10^{-6}$, $i = 0.1727481 \times 10^{-8}$.
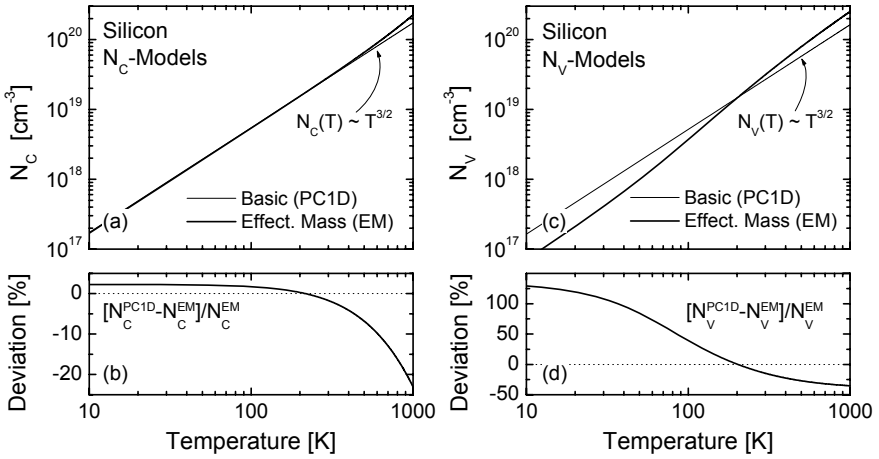
Fig. 1.7. Temperature dependence of the effective density of states (**a**) in the conduction band, $N_C(T)$, and (**c**) in the valence band, $N_V(T)$, for a basic *T*-model [*thin solid lines*, Eq. (1.4)] and an advanced *T*-model [*thick solid lines*, Eq. (1.26)] based on effective mass theory. The percentage deviation between the two models is shown for $N_C(T)$ and $N_V(T)$ in (**b**) and (**d**), respectively (*lower half*).

If Eqs. (1.27a) and (1.27b) are inserted in Eq. (1.26), explicit values for N_C and N_V can be calculated. The diagrams in the upper half of Fig. 1.7 display the temperature dependence of the effective densities of states in the conduction band, $N_C(T)$, and in the valence band, $N_V(T)$, respectively. To assess the relevance of the advanced $N_{C,V}$-model based on the effective mass theory (EM), both diagrams show the effective densities of states which result from the basic [thin solid lines, Eq. (1.4)] and the advanced model [thick solid lines, Eq. (1.26)][9]. In addition, the diagrams in the lower half of Fig. 1.7 display the percentage deviation between the models for $N_C(T)$ and $N_V(T)$, respectively.

As can be seen from Fig. 1.7a and b, up to 500 K the advanced EM model for $N_C(T)$ corresponds to the basic model within 5 % accuracy. While the overall temperature dependence of $N_C(T)$ approaches the $T^{1.5}$ power, as expected from Eq. (1.4), below 100 K, it is slightly enhanced in the intermediate temperature range from 200–500 K where it can be approximately described by a $T^{1.58}$ power law [8]. Only above 500 K, stronger deviations from the $T^{1.5}$-dependence have to be expected. Thus, in

---

[9]   Note that both $N_{C,V}$-models are used in current commercial semiconductor-device-simulation programs: while PC1D [6] uses the basic model, the advanced model is implemented in DESSIS [10].

the relevant temperature range from 100–600 K the impact of the advanced $N_C(T)$-model is expected to be of minor importance.

In contrast, the advanced EM model for $N_V(T)$ significantly differs from the basic model in terms of both absolute values and temperature dependence. As displayed in Fig. 1.7d, the deviation between the two models reaches 30 % in the relevant temperature range from 100–600 K and is even much higher at lower temperatures. Apart from that, Fig. 1.7c shows that the overall temperature dependence of $N_V(T)$ approaches the $T^{1.5}$ power expected from the simple model only at high (above 600 K) and low (below 50 K) temperatures while being strongly enhanced in the intermediate temperature range from 200–500 K, where it can be approximately described by a $T^{1.85}$ power law [8].

Thus, in the temperature range from 100–600 K, which is relevant to the investigations of the present work, the introduction of the advanced EM models for the effective densities of states will affect the fundamental semiconductor quantities particularly through $N_V(T)$ while the changes through $N_C(T)$ are of minor importance. This difference directly reflects the structural difference which has been observed in the temperature-dependent expressions (1.27a) and (1.27b) of the effective masses of electrons and holes.

B Definition of the advanced model

Analogously to the definition of the basic and standard model in Sects. 1.2.1C and 1.2.2C, we now define an *advanced model* for the temperature dependence of the fundamental semiconductor quantities. Since the advanced model is conceived as an extension of the standard model which additionally accounts for the temperature-dependence of the band gap and the effective masses, all the equations derived for the standard model hold good in the advanced model if only E_{gap} is replaced by $E_{gap}(T)$ from Eq. (1.25) and $N_C(T)$, $N_V(T)$ by the effective-mass-based models in Eq. (1.26). The set of semiconductor parameters used as defining basis for the advanced model is listed in Table 1.1 at the end of this chapter.

C Impact of the advanced model
on the basic semiconductor quantities

To assess the practical relevance of the advanced *T*-model, its impact on the basic semiconductor quantities should finally be investigated using derivations from Sect. 1.2.2. To visualize the impact of the advanced temperature models for $E_{gap}(T)$ and $N_{C,V}(T)$ alone, the different curves are each calculated twice in the following, under the assumption of the

standard (thin solid line) and the advanced *T*-model (thick solid line), and superposed in the same diagram. In addition, for some quantities the absolute deviation between the two models is plotted separately, which provides a quantitative estimate of the impact of the model extensions from Sect. 1.2.3A exclusively.

Their impact on the freeze-out effect is displayed in Fig. 1.8. Analogously to Fig. 1.2a, Fig. 1.8a shows the ionization degree f_A of boron atoms in silicon, whose temperature dependence has been calculated from Eq. (1.18) for different doping concentrations. As can be seen, the advanced *T*-model (thick solid lines) leads to a slight decrease in the ionization degree which directly reflects the fact that at low temperatures the density $N_V(T)$ of allowed states in the valence band is lower in the advanced than in the simple $N_V(T)$-model (see Fig. 1.7).[10] Showing the absolute deviation of the $f_A(T)$ curves for the two *T*-models, Fig. 1.8b reveals that the maximum f_A reduction due to the model exchange, which is given by the peak value, ranges from 10 to 6 % and decreases with increasing doping concentration.
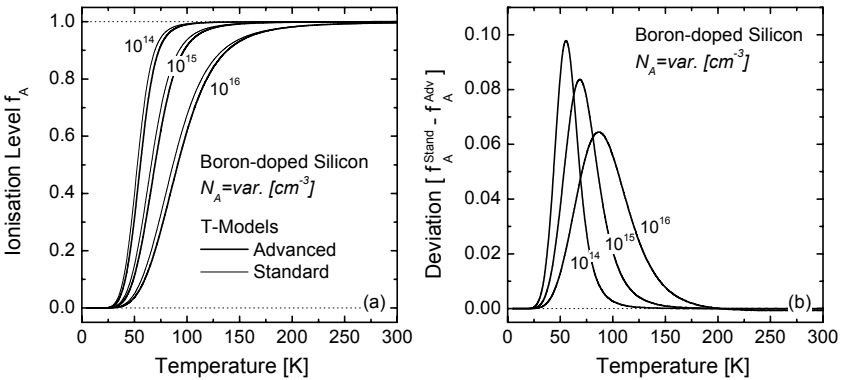
Fig. 1.8. Impact of the optimum advanced *T*-model on the freeze-out effect. (**a**) Ionization degree f_A of boron atoms in silicon calculated from Eq. (1.18) as a function of temperature for different doping concentrations under the assumption of the standard (*thin solid lines*) and the advanced *T*-model (*thick solid lines*). The advanced *T*-model leads to a slight reduction in the ionization degree. (**b**) Absolute deviation between corresponding $f_A(T)$ curves calculated for the two *T*-models.

---

[10]   An $E_{gap}(T)$ effect can be excluded since the doping level is assumed to be pinned to the adjacent band edge, its energy distance thus being temperature independent.
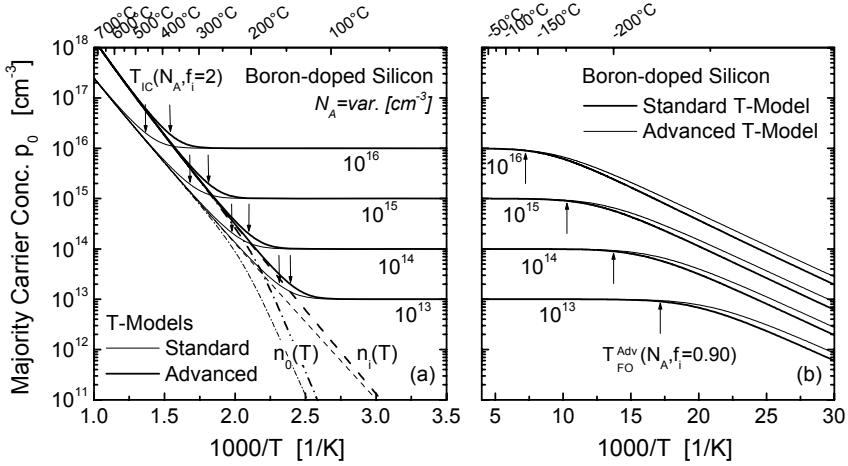
Fig. 1.9. Majority carrier concentration $p_0(T)$ in p-type silicon calculated from the composite model in Eq. (1.22) as a function of inverse temperature for different doping concentrations under the assumption of the standard (*thin solid lines*) and the advanced T-model (*thick solid lines*) for (**a**) high and (**b**) low temperatures. (**a**) At high temperatures the introduction of the advanced T-model induces an increase in the intrinsic carrier concentration $n_i(T)$ [*dashed line*, Eq. (1.5)] which is reflected in an onset of intrinsic conduction at lower temperatures. *Arrow pairs* indicate the IC onset temperatures T_{IC} for $f_i = 2$. (**b**) At low temperatures the advanced T-model induces a reduction of $p_0(T)$, which reflects the decrease in the ionization degree observed in Fig. 1.8.

Figure 1.9 displays the impact of the standard (thin solid line) and the advanced T-model (thick solid line) on the majority carrier concentration $p_0(T)$ in p-type silicon, which has been calculated as a function of inverse temperature for different doping concentrations using the composite model in Eq. (1.22). At low temperatures, as shown in Fig. 1.9b, the advanced T-model induces a reduction of $p_0(T)$ which directly reflects the decrease of the ionization degree observed in Fig. 1.8. The arrows in Fig. 1.9b indicate the temperatures T_{FO} for the onset of freeze-out which are determined for the advanced T-model and an f_A threshold of 0.90. Note that the T_{FO} values are hardly affected by the T-model.

At high temperatures, as shown in Fig. 1.9a, the introduction of the advanced T-model induces an increase in the intrinsic carrier concentration $n_i(T)$ (dashed lines) which is calculated from the defining Eq. (1.5). The increase in $n_i(T)$ comes mainly from the reduced band gap width (see Fig. 1.5) and to a lesser extent from the enhanced densities of states in the valence and the conduction band (see Fig. 1.8). Since the band gap width $E_{gap}(T)$ declines continuously with increasing temperature, the model-based difference in the magnitude of $n_i(T)$ grows continuously, which can

be seen from the divergence of the $n_i(T)$ curves for the standard (thin dashed line) and the advanced T-model (thick dashed line). The increase in $n_i(T)$ due to the model exchange is directly reflected in an onset of intrinsic conduction at lower temperatures. This is shown in Fig. 1.9a by the arrow pairs, which indicate for both T-models the onset temperatures of intrinsic conduction, T_{IC}, for an excitation degree $f_i = 2$.[11]

To allow the impact of the advanced T-model on intrinsic conduction to be assessed quantitatively, Fig. 1.10a displays the T_{IC} values, calculated from Eq. (1.21) on the basis of the advanced T-model, as a function of doping concentration for different transition factors f_i. If again $f_i = 1.10$ is defined as threshold for the transition to intrinsic conduction, the onset temperatures of intrinsic conduction range between 440 and 590 K in the relevant doping range from 10^{14} to 10^{16} cm^{-3}. Since the investigations of the present study are performed up to temperatures of 600 K, especially for the lesser doped samples a significant part of the investigated temperature range will be affected by intrinsic conduction, though the effect is present within the whole doping range. The enormous impact of only the advanced temperature models for $E_{gap}(T)$ and $N_{C,V}(T)$ becomes evident from Fig. 1.10b, which shows the absolute reduction of the onset temperatures T_{IC} due to the transition from the standard to the advanced T-model. As expected from the
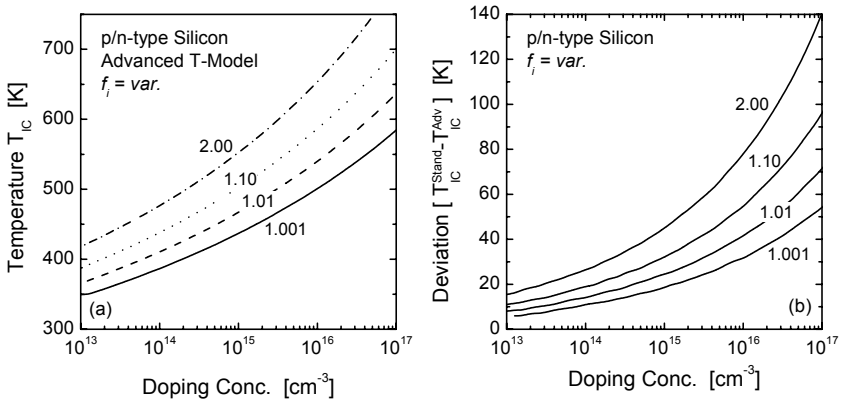
Fig. 1.10. (**a**) Onset temperature of intrinsic conduction T_{IC} calculated from Eq. (1.21) on the basis of the advanced T-model as a function of doping concentration for different transition factors f_i. (**b**) Absolute reduction of T_{IC} due to the transition from the standard to the advanced T-model as a function of doping concentration for different transition factors f_i.

---

[11]   The fact that the model-based distance between the onset temperatures increases with increasing doping concentration, even on the inverse temperature scale in Fig. 1.9a, indicates a superlinear grow of the T_{IC} reduction, which is consistent with the above observations on $n_i(T)$ and is shown explicitly in Fig. 1.10b.